SUPERCONDUCTIVITY

Superconducting phase diagram of multilayer square-planar nickelates

Grace A. Pan[1]†‡, Dan Ferenc Segedin[1]†, Sophia F. R. TenHuisen[1,2], Lopa Bhatt[3], Harrison LaBollita[4]§, Abigail Y. Jiang[1,2], Qi Song[1]¶, Ari B. Turkiewicz[1], Denitsa R. Baykusheva[1]#, Abhishek Nag[5]**, Stefano Agrestini[5], Ke-Jin Zhou[5]††, Jonathan Pelliciari[6], Valentina Bisogni[6], Hua Zhou[7], Mark P. M. Dean[8], Hanjong Paik[9]‡‡, David A. Muller[3,10], Lena F. Kourkoutis[3,10], Charles M. Brooks[1], Matteo Mitrano[1], Antia S. Botana[4], Berit H. Goodge[11], Julia A. Mundy[1,2]*

The discovery of superconductivity in square-planar nickelates has offered a rich materials platform to explore the origins of high-temperature superconductivity. However, experimental investigations have largely been limited to the infinite-layer $RNiO_2$ (R, rare earth) nickelates. We constructed a phase diagram of multilayer square-planar $Nd_{n+1}Ni_nO_{2n+2}$ compounds and found signatures of superconductivity for dimensionality $n = 4$ to 8. Upon decreasing n, the superconducting anisotropy evolves owing to 4f electron effects, and electronic structure characteristics approach cuprate-like behavior. Magnetic fluctuations persist from within the superconducting regime and into the overdoped, nonsuperconducting regime. The superconducting regime overlaps with that of chemically doped infinite-layer nickelates, demonstrating underlying commonalities as well as differences across varying structural realizations of square-planar nickelates. Our work establishes this layered template for creating new nickel-based superconductors.

After the discovery of high-temperature superconductivity in copper oxides (cuprates), there has been a longstanding search for similar superconductors (*1*–*4*). The nickel oxides (nickelates) have been an enduring candidate because Ni^{1+} and Cu^{2+} have the same $3d^9$ electron count (*5*, *6*). Superconductivity was eventually realized in thin films of Sr-doped $NdNiO_2$, the "infinite-layer" nickelate (Fig. 1A) (*7*). The superconducting nickelates have subsequently expanded to include infinite-layer $RNiO_2$ with various rare-earth (La, Pr, or Nd) and dopant (Sr, Ca, or Eu) cations (*8*–*11*), the five-layer square-planar $Nd_6Ni_5O_{12}$ (*12*), and electronically distinct perovskite-like nickelates (*13*). Despite the close analogy between square-planar nickelates and cuprates, there are key distinctions in their superconducting behavior, electronic structure, and correlated phases (*6*, *14*–*22*). This positions the square-planar nickelates as a rich materials class in which to explore unconventional superconductivity.

Underlying a broad structural and chemical diversity, the hole-doped cuprate phase diagrams exhibit distinct similarities in superconducting regions and in other proximate correlated features such as the strange metal, pseudogap, and Fermi-liquid–like phases (*2*, *23*, *24*). This universal phenomenology in the cuprates has motivated the pursuit of unifying theoretical descriptions, including especially effective spin-1/2 models on an antiferromagnetic square lattice. At the same time, the parameterization of cuprates by their subtle differences—such as apical oxygen-copper distances or the strength of orbital polarization—may help to distill the essential materials ingredients for high–critical temperature (T_c) superconductivity (*2*, *25*). Following this approach, key questions are which phenomenological features in the superconducting square-planar nickelates are similarly universal and thus reflect the basic physics of a d^9 nickel-oxygen system, and which features are sensitive to the precise structural environment and can be judiciously tuned.

We found a superconducting regime in the multilayer square-planar $Nd_{n+1}Ni_nO_{2n+2}$ compounds for dimensionality $n = 4$, 5, 6, 7, and 8 (Fig. 1D), tailoring the electronic properties in these chemically undoped compounds through structural layering. This superconducting regime overlaps with that of the chemically doped infinite-layer nickelates (*16*, *26*–*28*). We observed that the electronic structure becomes more cuprate-like with decreasing n (*15*, *29*, *30*).

Structural description of the multilayer square-planar nickelates

Multilayer $Nd_{n+1}Ni_nO_{2n+2}$ compounds are structurally analogous to electron-doped cuprates (such as $Nd_{2-x}Ce_xCuO_4$), which crystallize in the T′ structural form. Written schematically as $(NdNiO_2)_n(NdO_2)$, n layers of square-planar $NdNiO_2$ are hole doped by negatively charged $(NdO_2)^-$ fluorite spacer layers (Fig. 1A) to an average nominal doping value of $1/n$ holes per Ni^{1+} site (*6*, *31*–*33*). These multilayer square-planar nickelates can thus be directly mapped onto the phase diagram of the chemically doped $RNiO_2$ nickelates in terms of nominal electron count, providing a structural route to traverse the correlated phase space (Fig. 1A).

We synthesized thin-film $Nd_{n+1}Ni_nO_{2n+2}$ compounds for $n = 3$ to 8 following an improved version of the procedure we described previously (*12*, *34*–*36*). We began with the synthesis of epitaxial multilayer perovskite-like Ruddlesden-Popper type $Nd_{n+1}Ni_nO_{3n+1}$ compounds, followed by a topochemical reduction process that removed the apical oxygen and reduced the valence from $d^{7+1/n}$ to $d^{9-1/n}$. The large structural transformation between the Ruddlesden-Popper and multilayer square-planar phases, combined with additional rare-earth spacer layers (Fig. 1A) in multilayer nickelates, make this a particularly challenging synthesis (*34*, *35*, *37*). Nonetheless, we optimized this procedure to create the entire series for $n = 3$ to 10 (figs. S1 to S5) (*36*).

High-angle annular dark field scanning transmission electron microscopy (HAADF-STEM) of a representative $n = 6$ square-planar compound revealed a coherent atomic layered microstructure (Fig. 1, B and C). The overall defect density was greatly reduced compared with initial reports of the $Nd_6Ni_5O_{12}$ phase (fig. S5) (*12*, *36*). Smaller field-of-view HAADF-STEM and annular bright field (ABF)–STEM images revealed an atomically sharp $n = 6$ block and nickel-oxygen coordination representative of the square-planar phase (fig. S6) (*36*). Precise mapping of the intra-unit-cell lattice distances has shown that the out-of-plane Nd–Nd distances vary through the n-layer block (Fig. 1B and figs. S7 to S9) (*36*). The Nd–Nd distances are smaller in the interior of the n-layer block, approaching the c axis lattice constant of undoped $NdNiO_2$. Close to the fluorite $(NdO_2)^-$ layer, the Nd–Nd distance increases. The local lattice expansion near the fluorite layers, also captured by means of structural relaxations in density functional theory (DFT) calculations (*36*), could suggest that other properties such as

[1]Department of Physics, Harvard University, Cambridge, MA, USA. [2]John A. Paulson School of Engineering and Applied Sciences, Harvard University, Cambridge, MA, USA. [3]School of Applied and Engineering Physics, Cornell University, Ithaca, NY, USA. [4]Department of Physics, Arizona State University, Tempe, AZ, USA. [5]Diamond Light Source, Harwell Campus, Didcot, UK. [6]National Synchrotron Light Source II, Brookhaven National Laboratory, Upton, NY, USA. [7]X-ray Science Division, Advanced Photon Source, Argonne National Laboratory, Lemont, IL, USA. [8]Condensed Matter Physics and Materials Science Division, Brookhaven National Laboratory, Upton, NY, USA. [9]Platform for the Accelerated Realization, Analysis and Discovery of Interface Materials (PARADIM), Cornell University, Ithaca, NY, USA. [10]Kavli Institute at Cornell for Nanoscale Science, Cornell University, Ithaca, NY, USA. [11]Max Planck Institute for Chemical Physics of Solids, Dresden, Germany. ***Corresponding author. Email: mundy@fas.harvard.edu** †These authors contributed equally to this work. ‡Present address: Department of Materials Science and Engineering, University of Michigan, Ann Arbor, MI, USA. §Present address: Center for Computational Quantum Physics, Flatiron Institute, New York, NY, USA. ¶Present address: Department of Materials Science and Engineering, University of California, Irvine, CA, USA. #Present address: Institute of Science and Technology Austria, Klosterneuburg, Austria. **Present address: Department of Physics, Indian Institute of Technology Roorkee, Uttarakhand, India. ††Present address: National Synchrotron Radiation Laboratory and School of Nuclear Science and Technology, University of Science and Technology of China, Hefei, China. ‡‡Present address: School of Electrical and Computer Engineering and Center for Quantum Research and Technology, University of Oklahoma, Norman, OK, USA.

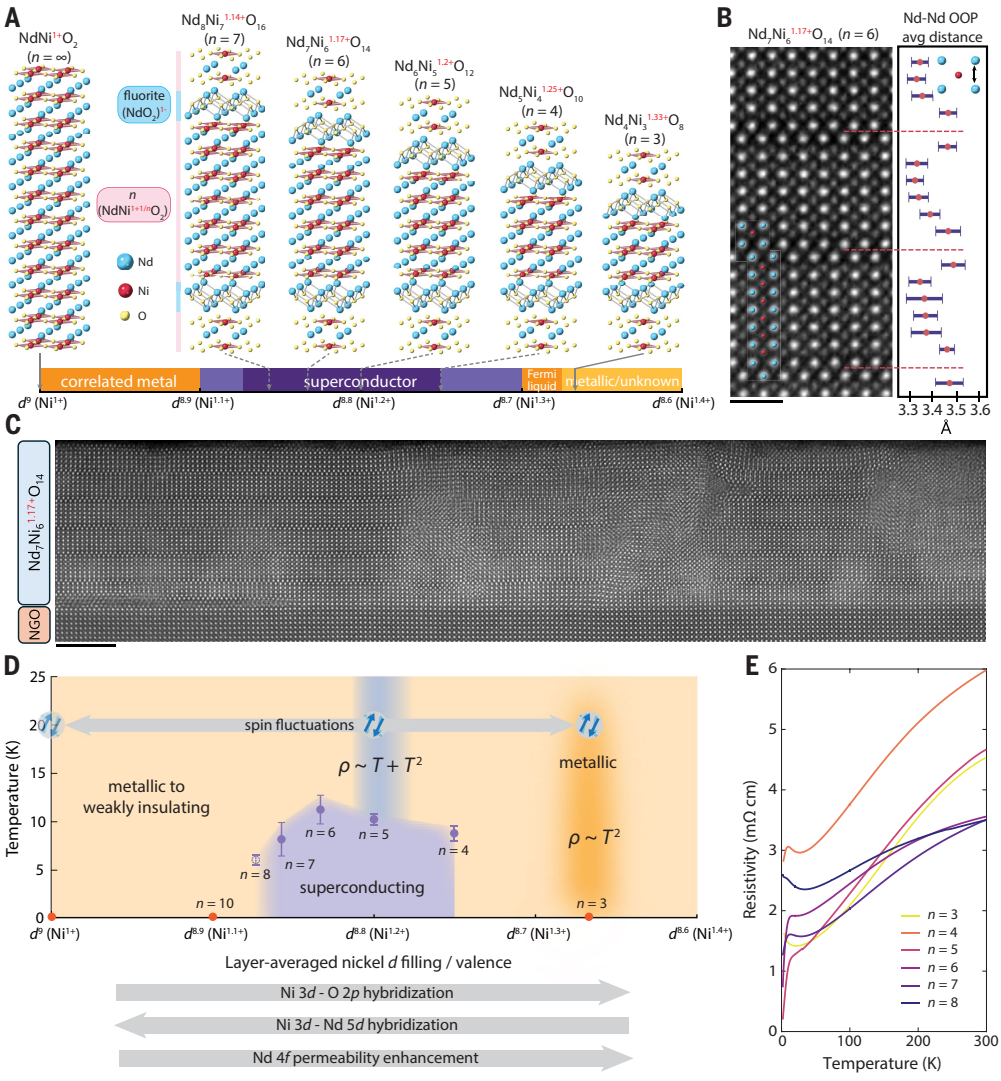

Fig. 1. Structure and correlated phase diagram of multilayer $Nd_{n+1}Ni_nO_{2n+2}$ nickelates. (**A**) Crystal structure schematic of the $Nd_{n+1}Ni_nO_{2n+2}$ compounds. *n* repeats of $NdNiO_2$ are sandwiched between charged $(NdO_2)^-$ fluorite layers. The fluorite layers soak up negative charge, nominally redistributing charge across the $NdNiO_2$ layers to $1/n$ holes per nickel. The compounds are mapped onto the doping-dependent phase diagram of the chemically doped $NdNiO_2$ nickelates. The dark purple range indicates the superconducting region taken from initial reports (*26*, *27*); light purple indicates the expanded superconducting region from recent improvements (*16*). Dashed lines indicate compounds that cannot be made through bulk synthesis methods. Teal, neodymium; red, nickel; yellow, oxygen. (**B**) HAADF-STEM image and Nd–Nd out-of-plane (OOP) lattice constant analysis of an $n = 6$ block. Dashed red lines indicate $(NdO_2)^-$ fluorite layers. The OOP Nd–Nd distance is larger close to the fluorite layers. Scale bar, 1 nm. (**C**) Large field-of-view STEM image of an $n = 6$ thin film on an $NdGaO_3$ substrate showing largely coherent microstructure. Scale bar, 5 nm. (**D**) Summarized phase diagram of the multilayer square-planar nickelates $Nd_{n+1}Ni_nO_{2n+2}$ as a function of nominal layer-averaged nickel *d*-electron count (nickel valence). Superconducting phase is indicated in purple; $T_{c,onset}$ was determined by using the criteria described in (*36*). The open circle for the $n = 8$ compound indicates superconducting correlations without a clear superconducting downturn. Blue arrow symbols indicate where spin fluctuations were identified with RIXS; the d^9 $(NdNiO_2)$ point is taken from (*54*). (Bottom) Gray arrows indicate the evolution of other properties discussed in this manuscript across the phase diagram. T^2 and *T*-linear labels are adapted from (*40*). (**E**) Resistivity of the $Nd_{n+1}Ni_nO_{2n+2}$ compounds for $n = 3$ to 8.

interlayer hopping or magnetic interactions may also be modified; we return to this point later in our discussion of magnetic excitations.

Characteristics of the superconducting state

We found signatures of superconducting transitions in the $n = 4$ to 7 compounds with onset of T_c ($T_{c,onset}$) ranging from 9.9 to 12.7 K (Fig. 1, D and E) and weak superconducting correlations in the $n = 8$ compound. This forms a region of superconducting behavior as a function of nominal nickel *3d* filling, or dimensionality *n*, corroborated by local spectroscopic measurements (fig. S10). The maximal observed $T_{c,onset}$ occurs at 12.7 K in $n = 6$, or a filling of $d^{8.83}$, which is approximately coincident in *d* filling with maximal T_c in recently optimized $Nd_{1-x}Sr_xNiO_2$ ($d^{8.825–8.85}$) (*16*). The $n = 4$ and $n = 8$ compounds—corresponding to $d^{8.75}$ and $d^{8.875}$, respectively—showed the weakest superconducting features, with superconducting downturns that lie on top of resistive upturn phases arising from localization or disorder-induced effects (Fig. 1E and figs. S11 and S12) (*36*). These effects, along with the broad superconducting transitions, have been observed in a variety of superconducting nickelates (*7*, *12*, *38*), including in multilayer nickelates $La_3Ni_2O_7$ (*39*) and $Nd_6Ni_5O_{12}$ (*38*, *40*). Hence, the $n = 4$ and $n = 8$ compounds likely represent the edges of the superconducting region accessible with dimensional doping.

The multilayer square-planar nickelates offer a distinctive structural knob to tune the electronic properties: Decreasing the layering order *n* should decrease the electronic dimensionality and enhance the two-dimensional (2D) behavior of the superconducting confinement (*12*, *41*). To this end, we interrogated the behavior of the superconducting transition in response to an applied magnetic field; a field applied perpendicular to the *a*-*b* plane should maximally—and a field applied parallel to the *a*-*b* plane should minimally—suppress the superconducting transition in a 2D system owing to orbital depairing effects (Fig. 2D) (*42*). Unexpectedly, in the most structurally 2D superconductor, $n = 4$, the superconducting anisotropy was minimal, whereas a less structurally 2D superconductor, $n = 6$, exhibited a stronger superconducting anisotropy (Fig. 2A).

We attribute this reversal of the expected superconducting anisotropy to the effect of the *4f* moments arising from the neodymium site (Fig. 2E), as originally proposed by (*29*). As suggested by the measurements in neodymium- or cerium-containing electron-doped cuprates (*43*, *44*), the *4f* moment on the rare-earth site forms an easy axis of enhanced magnetic permeability, increasing the paramagnetic depairing along the in-plane direction, which is typically the direction of minimal orbital depairing. This effect appears stronger with greater hole doping. Through angle-dependent magnetoresistive measurements (Fig. 2, B and F), we observed a general reversal of the expected superconducting anisotropy

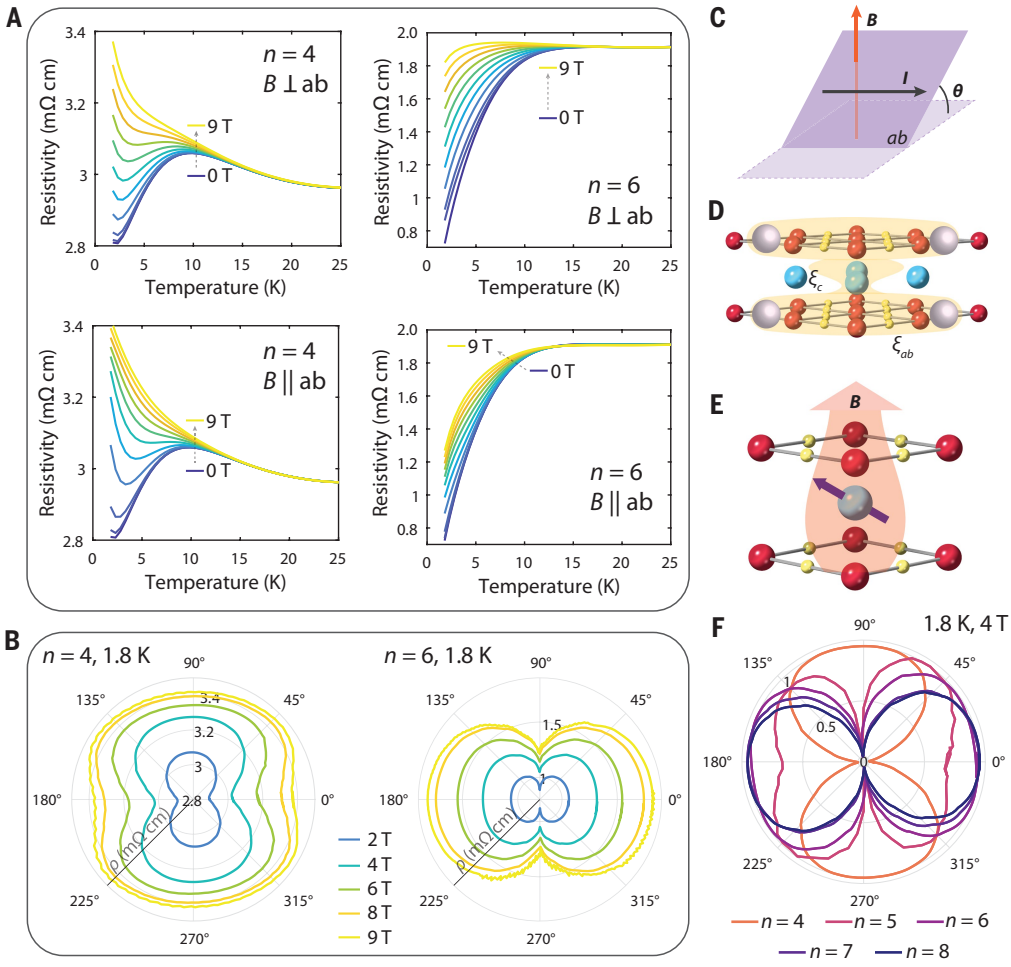

Fig. 2. Electronic transport characterization of the superconducting phases in $Nd_{n+1}Ni_nO_{2n+2}$. (**A**) Superconducting transitions of the $n = 4$ and $n = 6$ compounds, with magnetic fields applied in-plane or out-of-plane with respect to the sample surface. (Left) The $n = 4$ compound appears to behave isotropically in a magnetic field. (Right) The $n = 6$ compound shows a clear superconducting anisotropy. (**B**) Angle dependence of the magnetoresistance of the $n = 4$ and $n = 6$ compounds at 1.8 K. (**C**) Schematic of the measurement geometry. (**D**) A "typical" quasi-2D system would show strongly anisotropic orbital depairing from different coherence lengths. Gray spheres indicate electrons in Cooper pairs. The image is not to scale. (**E**) A system with 4*f* moment enhanced magnetic permeability. An external field applied out of plane would be internally enhanced (red) along moment directions. (**F**) Angle-dependent magnetoresistance of the $n = 4$ to 8 compounds at 1.8 K and 4 T. Data have been min-max normalized to display the changes in rotational anisotropy across all samples.

as we moved from $n = 8$ ($d^{8.875}$) to $n = 4$ ($d^{8.75}$) (fig. S13), which is consistent with observations in increasingly Sr-doped $NdNiO_2$.

In $Nd_{n+1}Ni_nO_{2n+2}$ nickelates, increased hole doping is achieved through a net increase of neodymium content from the additional $(NdO_2)^-$ layers, suggesting that the permeability enhancement could trivially arise from having more neodymium or from a closer structural proximity of the 4*f* moments in the $(NdO_2)^-$ layers to the Ni–O planes. However, in Sr-doped $NdNiO_2$, increased hole doping requires the removal of neodymium. Hence, the strength of the enhanced magnetic permeability from the 4*f* moment contribution likely does not principally derive from the neodymium content. This effect is also unrelated to the fragility of the superconducting phase; the "under-doped" $n = 8$ ($d^{8.875}$), which shows only weak superconducting correlations, shows weaker contributions from the 4*f* moments than those of the optimally and overdoped $n = 4$ to 6, which have sharper superconducting transitions. Last, our ability to synthesize the heavily overdoped, nonsuperconducting $Nd_4Ni_3O_8$ ($n = 3$, $d^{8.67}$) compound allows us to rule out this enhanced magnetic permeability as arising from nonsuperconducting impurity phases competing with the superconducting state. The nonsuperconducting $n = 3$ compound exhibits a very weak twofold resistivity anisotropy that likely originates from localization effects and is 90° out of phase with the feature generated by this paramagnetic depairing mechanism (figs. S14 and S15) (*36*).

Combined, these observations suggest an underlying commonality within the nickelate phase diagram: The permeability enhancement by the neodymium 4*f* moment increases with increased hole doping in the superconducting region. The impact of the 4*f* moments is strong enough to completely obscure the effects of dimensional reduction through structural tuning. The $R_{n+1}Ni_nO_{2n+2}$ compounds are therefore optimal systems to study the interplay of superconducting dimensionality effects with rare-earth magnetism. By selectively tuning the rare-earth composition (R = La, Pr, or Nd) in $R_{n+1}Ni_nO_{2n+2}$, one could potentially isolate the impact of the 4*f* moments on the superconducting state and tune the magnetic interactions in lower dimensions (*29*, *45*). To this end, we have synthesized the $La_{n+1}Ni_nO_{2n+2}$ compounds, which have no *f* electrons but are not superconducting to date, possibly owing to strain-driven synthesis effects (figs. S17 to S21) (*36*).

Electronic structure

A notable difference between cuprates and square-planar nickelates lies in their electronic structures (Fig. 3A). Cuprates can largely be described as charge-transfer insulators with an effective single band derived from hybridized *p*-*d* oxygen-copper states. By contrast, nickelates show reduced *p*-*d* oxygen-nickel hybridization and additional rare-earth 5*d* bands close to the Fermi level, which may potentially self-dope the system, hybridize electronically with the nickel 3*d* bands, or even generate Kondo states (*14*, *18*, *46*–*48*). However, we found with DFT calculations that in the $Nd_{n+1}NinO_{2n+2}$ nickelates, lower n nickelates should recover more cuprate-like features, with decreased 5*d*-3*d* (rare earth–nickel) hybridization and increased 2*p*-3*d* (oxygen-nickel) hybridization (Fig. 3B and fig. S22) (*36*). To experimentally assess the evolution of electronic structure characteristics with n in the $Nd_{n+1}Ni_nO_{2n+2}$ compounds, we used resonant inelastic x-ray scattering (RIXS) at the nickel L_3 edge (figs. S25 and S26).

Representative RIXS spectra taken for the $n = 3$ and $n = 5$ compounds are shown in Fig. 3C. Both samples show orbital excitations consistent with square-planar oxygen coordination of nickel sites: a peak at 1.4 eV energy loss from d_{xy} orbitals, a peak at 2 eV from d_{xz}/d_{yz} orbitals, and a higher energy shoulder from $d_{3z^2-r^2}$ orbitals as has been established in $RNiO_2$ (*30*). Above 5 eV, we observed a broad, higher-energy feature that we attribute to Ni–O hybridization (*21*, *49*, *50*). This

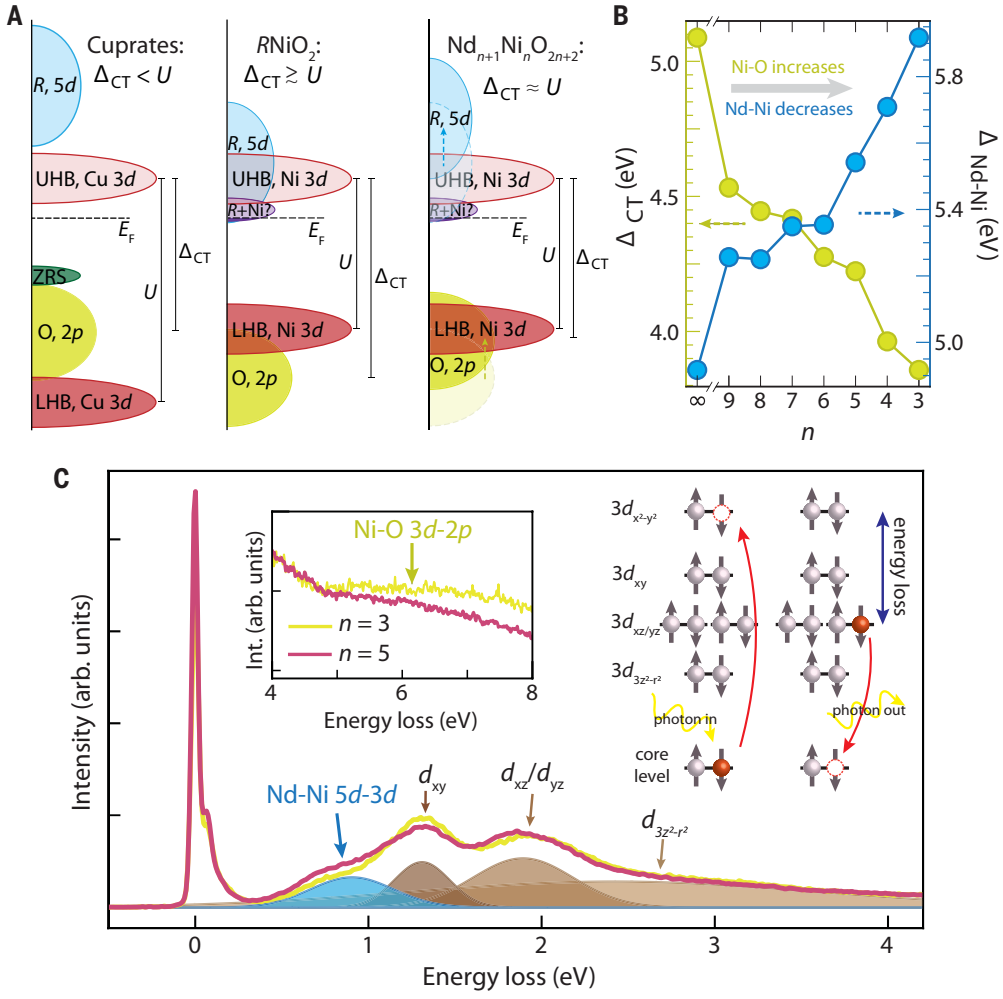

Fig. 3. Electronic structure characterization of the $Nd_{n+1}Ni_nO_{2n+2}$. (**A**) Cartoon electronic structure diagrams of the (left) cuprates, (middle) RNiO$_2$ nickelates, and (right) $Nd_{n+1}Ni_nO_{2n+2}$. The dashed lines indicating changes in the $Nd_{n+1}Ni_nO_{2n+2}$ diagram are relative to NdNiO$_2$ as n decreases. U, Mott-Hubbard on-site repulsion; Δ_{CT}, charge-transfer gap; LHB, lower Hubbard band; UHB, upper Hubbard band; ZRS, Zhang-Rice singlet. R+Ni is the rare earth–nickel interaction whose electronic nature is unresolved. (**B**) DFT predictions, derived from centroids of the atom-resolved density of states (*36*), of the charge-transfer gap (Δ_{CT}) and the neodymium-nickel hybridization gap (Δ_{Nd-Ni}). Increasing gap size corresponds to decreasing hybridization strength. (**C**) Sample RIXS spectrum of the n = 3, 5 compounds at $q_{||}$ = (−0.45, 0). Orbital excitations are indicated with the colored peaks. (Left inset) High energy loss feature corresponding to Ni–O hybridization. (Right inset) Schematic of the RIXS process that generates *dd*-excitations in a square-planar crystal field.

feature is stronger in the n = 3 than in the n = 5 compound, corroborating a Ni–O hybridization increase with decreasing n. At ~0.7 eV, we observed a lower energy shoulder that we attribute to Nd–Ni hybridization, which has also been observed in (*18*, *30*, *51*). This feature is weaker in the n = 3 compound than the n = 5 compound relative to the *dd* orbital excitations, affirming that Nd–Ni hybridization decreases with decreasing dimensionality (*12*, *41*, *52*).

Together, these observations reinforce the DFT calculations (Fig. 3B) (*36*, *41*) that show that hole doping from $3d^9$, whether through chemical doping or dimensional tuning, enhances the cuprate-like electronic structure in square-planar nickelates (*53*). In this context, it is notable that overdoped n = 3 and 32.5% Sr-doped NdNiO$_2$ do not superconduct. An open challenge then is to identify the features associated with the destruction of superconductivity in the nickelates.

Magnetic excitations

One common candidate for superconducting pairing is the magnetic interaction. In cuprates, superconductivity emerges upon doping a long-range ordered antiferromagnetic (AFM) phase. By contrast, no long-range AFM order has been observed in underdoped nickelates, although spin fluctuations and signatures of a spin glass phase have been reported in the underdoped and optimally doped infinite-layer nickelates (*22*, *54*). We explored the highly overdoped side of the phase diagram beyond what has been achieved with chemical substitution.

Our principal finding is the observation through momentum-resolved RIXS (Fig. 4, A and B) of damped magnetic excitations at ~80 meV in superconducting n = 5 ($d^{8.8}$) (Fig. 4, C to E), which persists past superconductivity well into overdoped, metallic n = 3 ($d^{8.67}$) (*36*). We identified these inelastic features as having a magnetic origin through the incident energy and polarization dependence of the RIXS spectra (figs. S27 and S28) (*36*). Furthermore, the broadness and amplitude of the feature is inconsistent with a phononic origin (fig. S27) (*36*). The magnetic features in both n = 3 and n = 5 compounds can be well-modeled by a single magnetic branch (Fig. 4C) and lack a strong dispersion in momentum along the (h, 0) direction (Fig. 4D). We did not observe notable differences in the excitations between the samples other than a slight increase of the damping near the zone boundary in the n = 3 compound, which is consistent with its more metallic nature. This contrasts with the chemically doped infinite-layer nickelates, which have more dispersive features with a damping and mode energy that change more substantially with doping (*54*). Given the similarity of the spectra between the nonsuperconducting n = 3 and the superconducting n = 5 compounds then, the relationship between these magnetic modes and superconductivity is unclear.

One possibility is that the structural form of the $Nd_{n+1}Ni_nO_{2n+2}$ nickelates directly affects these relatively unchanging spin excitation features. The presence of the fluorite layers, which cause a local lattice expansion of the outermost Ni–O planes, identified by our lattice constant analysis with STEM (Fig. 1B), may reflect changes in the magnetic unit cell (fig. S24 and table S2) relative to NdNiO$_2$ and give rise to multiple magnon modes n within a single compound, similar to what was observed in bulk $La_4Ni_3O_8$ and $Pr_4Ni_3O_8$ (*55*). These magnon modes are likely all strongly damped and further blurred by the

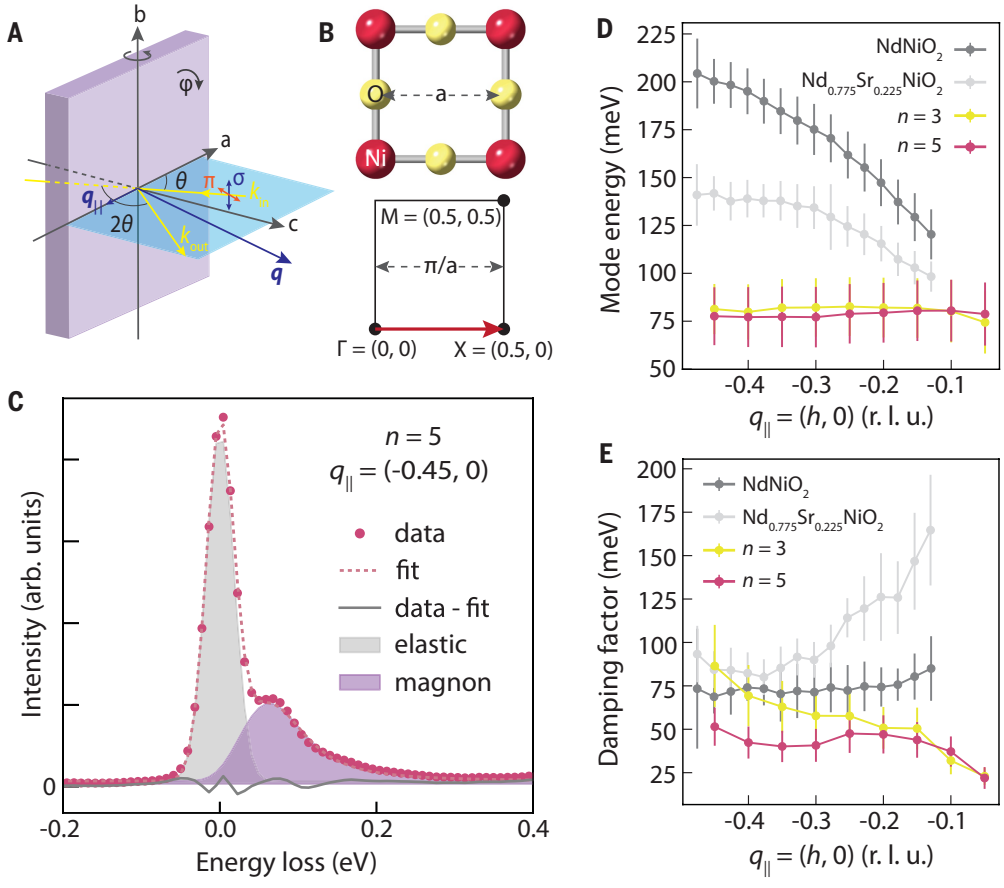

Fig. 4. Magnetic excitations in $Nd_{n+1}Ni_nO_{2n+2}$ using RIXS. (**A**) Schematic of the RIXS scattering geometry used to access trajectories in momentum space. Purple indicates the sample, and blue indicates the scattering plane. (**B**) Real- and momentum-space cartoons of the direction of the momentum scan direction in (D) and (E). (**C**) Example low-energy loss spectrum highlighting the magnon-derived contribution. (**D**) Energy and (**E**) damping terms of the magnetic excitation along the $q_{||} = (h, 0)$ direction of the $n = 3, 5$ nickelates, compared with infinite-layer nickelates. Infinite-layer nickelate data are from (*54*).

spectrometer resolution and thus cannot be individually resolved. Consequently, we observed an average of all the $2n$ magnetic branches, with different weights throughout the Brillouin zone (*55*). Hence, ~80 meV represents a lower bound for the magnetic energy scales in this family of materials (*36*). This is comparable with the minimum observed for chemically doped infinite-layer nickelates and is of a magnitude similar to that of the energy scales observed in many cuprates (*56*–*58*).

We reiterate that in either scenario, magnetic excitations persist well into the overdoped, nonsuperconducting side of the nickelate phase diagram. Although this persistence is similar to cuprates (*57*), unlike in cuprates, the destruction of superconductivity here is not necessarily associated with a weakening of the magnetic interaction a priori; the $n = 3$ compound appears more like superconducting cuprates in oxygen hybridization, quasi–two-dimensionality, and reduced role of the rare-earth band (Fig. 3), although it is not superconducting. Future studies attempting to identify the role of magnetism or high hole doping in nickelates, or to relate T_c to the strength of magnetic interactions, could leverage a combination of chemical doping in multilayer square-planar nickelates of varying n throughout the superconducting region.

Discussion and outlook

Combined, we constructed a distinct phase diagram for multilayer square-planar nickelates $Nd_{n+1}Ni_nO_{2n+2}$ (Fig. 1D). The superconducting regime heavily overlaps in nominal electron count with chemically doped infinite-layer nickelates and hole-doped cuprates, indicating that square-planar nickelate superconductivity occurs over an apparently universal doping range near $3d^9$.

The electronic structure trends are consistent with hole-doping in infinite-layer nickelates and bring lower-n layered nickelates closer to the cuprates. As n is decreased, rare-earth $5d$ hybridization decreases, and oxygen $2p$ hybridization increases, reaffirming the emergence of cuprate-like properties in lower-dimensional square-planar structures. Furthermore, the distinct role of neodymium $4f$ moments in infinite-layer nickelates is reprised in multilayer $Nd_{n+1}Ni_nO_{2n+2}$ nickelates. The magnetic character of the $4f$ moments alters the superconducting anisotropy contrary to what is expected with increased confinement in a thin-film geometry. This effect increases with increasing hole doping whether through chemical doping or structural tuning by decreasing n, indicating that it evolves universally in square-planar nickelates.

There also are distinctions between the multilayer square-planar nickelates and their infinite-layer counterparts. First, the effects of neodymium $4f$ moments unexpectedly wash out the expected enhancement of superconducting anisotropy as n is decreased. This points to a complex interplay between the role of rare-earth magnetism and dimensionality in the superconducting phase of these multilayer systems, which may be tunable with future realization of superconductivity in $R_{n+1}Ni_nO_{2n+2}$ compounds of different rare-earth cations.

Furthermore, structural tuning allows us to access high doping ranges and hence track the evolution of spin fluctuations deep into the overdoped regime of multilayer $Nd_{n+1}Ni_nO_{2n+2}$ nickelates. Magnetic excitations persist from superconducting $n = 5$ to highly overdoped, metallic $n = 3$ compounds with minimal modification. This resembles the persistence of magnetic excitations in cuprates through the overdoped regime (*57*), although the relationship between these magnetic modes and superconductivity is presently unclear.

Another key distinction between the multilayer nickelates and their infinite-layer counterparts is the structural inequivalence between the individual n $NdNiO_2$ layers as observed with STEM (Fig. 1B) (*36*). This may lead to a layer-dependent modulation of other properties—including, for example, an interpretation of the spin fluctuation dispersion in RIXS as emerging from multiple magnon branches (*55*, *59*). Additionally, in multilayer cuprates, experimental mapping of the band structure suggests that a variation of properties across multiple layers can explain trends in T_c (*60*, *61*). Our observed lattice modulation provides evidence toward layer-dependent properties, which may be identified in the future as advancements in STEM–electron energy-loss spectroscopy (EELS) move toward atomic-level resolution of subtle spectroscopic features (*62*). This also underscores the role of the spacer layer; the steric effect is subtle in the case of $(NdO_2)^-$ fluorite layers, but we posit that such spacer layers

can be more broadly functionalized. This could involve chemical doping or intercalation to tune structural distortions, which in turn may modify interlayer couplings, magnetic interactions, chemical pressure, anion coordination, and electronic correlations (*52*).

Last, the *d*-filling–dependent superconducting regime of the multilayer nickelates overlaps with that of the infinite-layer compounds, which apparently unifies the square-planar nickelates across different structural realizations. This is notable considering the structural distinctions, the subtle modifications to magnetic excitations, and even the empirical uncertainties in oxygen stoichiometry (*17*, *63*, *64*). Hence, the multilayer square-planar nickelates give us a structurally distinct platform to help distill the ingredients of nickelate superconductivity and examine fundamental theories, including the role of Kondo coupling (*47*). Experimentally, we can expect atomic-level design to target new superconducting nickelates. This may include synergizing chemical substitution with structural tuning to enhance T_c or to determine its precise functional dependence on hole doping and, within the shared $3d^9$ doping range, could extend beyond the square planar motif.

REFERENCES AND NOTES

1. J. G. Bednorz, K. A. Müller, *Z. Phys. B Condens. Matter* **64**, 189–193 (1986).
2. B. Keimer, S. A. Kivelson, M. R. Norman, S. Uchida, J. Zaanen, *Nature* **518**, 179–186 (2015).
3. A. P. Mackenzie, Y. Maeno, *Rev. Mod. Phys.* **75**, 657–712 (2003).
4. F. Wang, T. Senthil, *Phys. Rev. Lett.* **106**, 136402 (2011).
5. V. I. Anisimov, D. Bukhvalov, T. M. Rice, *Phys. Rev. B Condens. Matter* **59**, 7901–7906 (1999).
6. J. Zhang *et al.*, *Nat. Phys.* **13**, 864–869 (2017).
7. D. Li *et al.*, *Nature* **572**, 624–627 (2019).
8. S. Zeng *et al.*, *Sci. Adv.* **8**, eabl9927 (2022).
9. M. Osada *et al.*, *Nano Lett.* **20**, 5735–5740 (2020).
10. M. Osada *et al.*, *Adv. Mater.* **33**, e2104083 (2021).
11. W. Wei, D. Vu, Z. Zhang, F. J. Walker, C. H. Ahn, *Sci. Adv.* **9**, eadh3327 (2023).
12. G. A. Pan *et al.*, *Nat. Mater.* **21**, 160–164 (2022).
13. H. Sun *et al.*, *Nature* **621**, 493–498 (2023).
14. A. S. Botana, M. R. Norman, *Phys. Rev. X* **10**, 011024 (2020).
15. B. H. Goodge *et al.*, *Proc. Natl. Acad. Sci. U.S.A.* **118**, e2007683118 (2021).
16. K. Lee *et al.*, *Nature* **619**, 288–292 (2023).
17. C. T. Parzyck *et al.*, *Nat. Mater.* **23**, 486–491 (2024).
18. M. Hepting *et al.*, *Nat. Mater.* **19**, 381–385 (2020).
19. M. Rossi *et al.*, *Nat. Phys.* **18**, 869–873 (2022).
20. C. C. Tam *et al.*, *Nat. Mater.* **21**, 1116–1120 (2022).
21. Y. Shen *et al.*, *Phys. Rev. X* **12**, 011055 (2022).
22. J. Fowlie *et al.*, *Nat. Phys.* **18**, 1043–1047 (2022).
23. H. Zhang, H. Sato, *Phys. Rev. Lett.* **70**, 1697–1699 (1993).
24. P. W. Phillips, N. E. Hussey, P. Abbamonte, *Science* **377**, eabh4273 (2022).
25. L. F. Feiner, M. Grilli, C. Di Castro, *Phys. Rev. B Condens. Matter* **45**, 10647–10669 (1992).
26. D. Li *et al.*, *Phys. Rev. Lett.* **125**, 027001 (2020).
27. S. Zeng *et al.*, *Phys. Rev. Lett.* **125**, 147003 (2020).
28. B. Y. Wang, K. Lee, B. H. Goodge, *Annu. Rev. Condens. Matter Phys.* **15**, 305–324 (2024).
29. B. Y. Wang *et al.*, *Sci. Adv.* **9**, eadf6655 (2023).
30. M. Rossi *et al.*, *Phys. Rev. B* **104**, L220505 (2021).
31. P. Lacorre, *J. Solid State Chem.* **97**, 495–500 (1992).
32. V. V. Poltavets *et al.*, *J. Am. Chem. Soc.* **128**, 9050–9051 (2006).
33. V. V. Poltavets *et al.*, *Inorg. Chem.* **46**, 10887–10891 (2007).
34. D. Ferenc Segedin *et al.*, *Nat. Commun.* **14**, 1468 (2023).
35. G. A. Pan *et al.*, *Phys. Rev. Mater.* **6**, 055003 (2022).
36. Materials and methods are available as supplementary materials.
37. K. Lee *et al.*, *APL Mater.* **8**, 041107 (2020).
38. X. Yan *et al.*, *Sci. Adv.* **11**, eado4572 (2025).
39. E. K. Ko *et al.*, *Nature* **638**, 935–940 (2025).
40. G. Grissonnanche *et al.*, *Phys. Rev. X* **14**, 041021 (2024).
41. H. LaBollita, A. S. Botana, *Phys. Rev. B* **104**, 035148 (2021).
42. M. Tinkham, *Introduction to Superconductivity* (Courier Corporation, 2004).
43. R. Prozorov, R. W. Giannetta, P. Fournier, R. L. Greene, *Phys. Rev. Lett.* **85**, 3700–3703 (2000).
44. J. W. Lynn *et al.*, *Phys. Rev. B Condens. Matter* **41**, 2569–2572 (1990).
45. L. E. Chow *et al.*, arXiv:2301.07606 [cond-mat.supr-con] (2023).
46. F. Lechermann, *Phys. Rev. B* **101**, 081110 (2020).
47. G.-M. Zhang, Y. Yang, F.-C. Zhang, *Phys. Rev. B* **101**, 020501 (2020).
48. E. Been *et al.*, *Phys. Rev. X* **11**, 011050 (2021).
49. Y. Shen *et al.*, *Phys. Rev. X* **13**, 011021 (2023).
50. M. R. Norman *et al.*, *Phys. Rev. B* **107**, 165124 (2023).
51. G. Krieger *et al.*, *Phys. Rev. Lett.* **129**, 027002 (2022).
52. P. Worm *et al.*, *Phys. Rev. Mater.* **6**, L091801 (2022).
53. J. Krishna, H. LaBollita, A. O. Fumega, V. Pardo, A. S. Botana, *Phys. Rev. B* **102**, 224506 (2020).
54. H. Lu *et al.*, *Science* **373**, 213–216 (2021).
55. J. Q. Lin *et al.*, *Phys. Rev. Lett.* **126**, 087001 (2021).
56. M. Le Tacon *et al.*, *Nat. Phys.* **7**, 725–730 (2011).
57. M. P. M. Dean *et al.*, *Nat. Mater.* **12**, 1019–1023 (2013).
58. Y. Y. Peng *et al.*, *Nat. Phys.* **13**, 1201–1206 (2017).
59. J. Zhang *et al.*, *Nat. Commun.* **11**, 6003 (2020).
60. S. Kunisada *et al.*, *Science* **369**, 833–838 (2020).
61. X. Luo *et al.*, *Nat. Phys.* **19**, 1841–1847 (2023).
62. M. Colletta, R. Chang, I. El Baggari, L. F. Kourkoutis, *Microsc. Microanal.* **29** (suppl. 1), 394–396 (2023).
63. C. T. Parzyck *et al.*, *Phys. Rev. X* **15**, 021048 (2025).
64. H. Sahib *et al.*, *Adv. Mater.* **37**, e2416187 (2025).
65. G. Kresse, J. Hafner, *Phys. Rev. B Condens. Matter* **47**, 558–561 (1993).
66. G. Kresse, J. Furthmüller, *Phys. Rev. B Condens. Matter* **54**, 11169–11186 (1996).
67. G. Kresse, D. Joubert, *Phys. Rev. B Condens. Matter* **59**, 1758–1775 (1999).
68. G. Pan, Replication data for: Superconducting phase diagram of multi-layer square-planar nickelates. *Harvard Dataverse* (2026); https://doi.org/10.7910/DVN/YW10CE

ACKNOWLEDGMENTS

We thank S. Novakov and J. T. Heron for electronic measurement assistance; D. A. Walko for assistance with surface x-ray diffraction experiments at the Advanced Photon Source; and G. Grissonnanche and B. J. Ramshaw for helpful discussions. **Funding:** This project was primarily supported by the US Department of Energy (DOE), Office of Basic Energy Sciences, Division of Materials Sciences and Engineering under award DE-SC0021925. Materials growth and electron microscopy were supported in part by the Platform for the Accelerated Realization, Analysis, and Discovery of Interface Materials (PARADIM) under NSF Cooperative Agreement DMR-2039380. Electron microscopy was primarily performed at the Cornell Center for Materials Research shared facilities, which are supported by the NSF MRSEC program DMR-1719875. All nanofabrication work was performed at Harvard University's Center for Nanoscale Systems, a member of the National Nanotechnology Coordinated Infrastructure Network supported by NSF award ECCS-2025158. The RIXS measurements and their interpretation by S.F.R.T., V.B., M.P.M.D., and M.M. was supported by the DOE Division of Materials Science under contract DE-SC0012704. RIXS was performed in part at Diamond Light Source on beamline I21-RIXS under proposal MM27484. This research used beamline 2-ID of NSLS-II, a DOE Office of Science User Facility operated for the DOE Office of Science by Brookhaven National Laboratory under contract DE-SC0012704. Synchrotron surface x-ray diffraction measurements were performed under beam time award Rapid Access GUP-1013484 (https://doi.org/10.46936/APS-189299/60013669) at sector 7-ID-C at the Advanced Photon Source, a DOE Office of Science user facility operated for the DOE Office of Science by Argonne National Laboratory under contract DE-AC02-06CH11357. G.A.P., D.F.S., and A.Y.J. acknowledge support from the NSF Graduate Research Fellowship grant DGE-1745303. G.A.P. and A.Y.J. were also supported by the Paul & Daisy Soros Fellowship for New Americans, and A.Y.J. was also supported by the Ford Foundation. A.B.T. was supported by NSF grant DMR-2323970. A.S.B. acknowledges NSF grant DMR-2323971 and the ASU Research Computing Center for HPC resources. H.L. acknowledges NSF grant DMR-2045826. L.B., B.H.G., and L.F.K. acknowledge support from PARADIM, NSF DMR-2039380. B.H.G. was also supported by the Schmidt Science Fellows in partnership with the Rhodes Trust. J.A.M. acknowledges support from the Packard Foundation, Sloan Foundation, and the Gordon and Betty Moore Foundation's EPiQS Initiative, grant GBMF6760. **Author contributions:** G.A.P, A.S.B., and J.A.M. conceived of and designed the experiment. G.A.P. and D.F.S. synthesized the samples using oxide molecular beam epitaxy, with contributions from A.Y.J., Q.S., A.B.T., H.P., C.M.B, and J.A.M.; G.A.P. and D.F.S. performed reductions and diffraction. G.A.P. performed transport experiments, with contributions from D.F.S.; L.B. and B.H.G. performed and analyzed STEM and EELS measurements, with support from L.F.K. and D.A.M.; S.F.R.T, G.A.P, and D.R.B conducted RIXS experiments and analysis, with support from A.N., S.A., K.-J.Z., J.P., V.B., M.P.M.D., and M.M.; D.F.S. and H.Z. performed synchrotron x-ray diffraction. H.L. and A.S.B. performed density functional theory calculations. G.A.P. wrote the manuscript, with input from all authors. J.A.M. supervised the project. **Competing interests:** The authors declare that they have no competing interests. **Data, code, and materials availability:** DFT calculations were performed by using the Vienna Ab initio Simulation Package (VASP) code (*65*–*67*). All data in the main text and the supplementary materials are available in the Harvard Dataverse (*68*). Details for the synthesis and characterization of all materials are in the supplementary materials, materials and methods.

SUPPLEMENTARY MATERIALS

science.org/doi/10.1126/science.adp4440
Materials and Methods; Supplementary Text; Figs. S1 to S32; Tables S1 and S2; References (*69*–*125*)

Submitted 2 July 2024; resubmitted 23 May 2025; accepted 30 April 2026

10.1126/science.adp4440

Superconducting phase diagram of multilayer square-planar nickelates

Grace A. Pan, Dan Ferenc Segedin, Sophia F. R. TenHuisen, Lopa Bhatt, Harrison LaBollita, Abigail Y. Jiang, Qi Song, Ari B. Turkiewicz, Denitsa R. Baykusheva, Abhishek Nag, Stefano Agrestini, Ke-Jin Zhou, Jonathan Pelliciari, Valentina Bisogni, Hua Zhou, Mark P. M. Dean, Hanjong Paik, David A. Muller, Lena F. Kourkoutis, Charles M. Brooks, Matteo Mitrano, Antia S. Botana, Berit H. Goodge, and Julia A. Mundy

Science **392** (6805), . DOI: 10.1126/science.adp4440

Editor's summary

Superconductivity in the nickelates, layered compounds with notable similarities to the cuprates, can be tuned by chemical doping and by applying pressure. Pan *et al*. used a different approach: varying the number of $NdNiO_2$ layers (n) sandwiched between NdO_2 layers, synthesizing a series of $Nd_{n+1}Ni_nO_{2n+2}$ compounds. This structural tuning enabled the researchers to access a large range of behaviors, including that of cuprate-like materials at smaller n. — Jelena Stajic